UCSF

UC San Francisco Previously Published Works

Authors

Gullberg, Grant T
Shrestha, Uttam
Kim, Sally Ji Who
et al.

X-ray Bi-prism Interferometry – A Design Study of Proposed Novel Hardware

Grant T. Gullberg,[1] Uttum Shrestha,[1] Sally Ji Who Kim,[2] Youngho Seo,[1] Michael Fuller[3]

[1]Department of Radiology and Biomedical Imaging, University of California San Francisco, San Francisco, CA 94143-0946, USA

[2]Cardiovascular Research Center, Massachusetts General Hospital, Harvard Medical School, Boston, MA 02114, USA

[3]TF Instruments, Salinas, CA 93908, USA

Corresponding author: Grant T. Gullberg

Department of Radiology and Biomedical Imaging

University of California San Francisco, San Francisco, CA 94143-0946, USA

Email: gtgullberg@lbl.gov

Phone: (510) 525-1964

Running Title: X-ray Bi-prism Interferometry

Abstract

Purpose: Advances in X-ray phase-contrast imaging can obtain excellent soft-tissue contrast of phase-shift, attenuation, and small angle scatter. Here we present fringe patterns for different design parameters of X-ray bi-prism interferometry imaging systems. Our aim is to develop bi-prism interferometry imaging systems with excellent polychromatic performance that produce high-contrast fringes with spatially incoherent X-ray illumination. We also introduce a novel X-ray tube design that uses temporal multiplexing to provide simultaneous virtual "electronic phase stepping" that replace "mechanical phase stepping" popular with grating-based interferometry setups.

Methods: In our investigation we develop expressions for the irradiance distribution pattern of a bi-prism interferometer comprised of multiple point sources and multiple bi-prisms. These expressions are used to plot fringe patterns for X-ray design parameters including size of point source, number of point sources, and point source separation; and bi-prism design parameters including material, angle, number of bi-prisms, period, and bi-prism array to X-ray source and to detector distances.

Results: Results show that the fringe patterns for a bi-prism interferometry system are not longitudinally periodic as with grating interferometers that produce a Talbot-Lau carpet. It is also shown that at 59 keV X-rays the bi-prism material should be something comparable to nickel to obtain reasonable fringe visibility.

Conclusion: The irradiance distribution pattern demonstrates that bi-prism interferometry may provide comparable or improved fringe visibility to that of gratings. Special care is given to present our findings within the context of previous advancements. A single-shot image acquisition approach using a temporal multiplexed, high-power X-ray source provides virtual electronic phase stepping without focal spot sweeping. This provides multiple images, each at the same exposure and the same projection view, from different fringe locations that allow one to derive the attenuation, phase, and dark-field images of the sample without mechanical phase stepping of a grating.
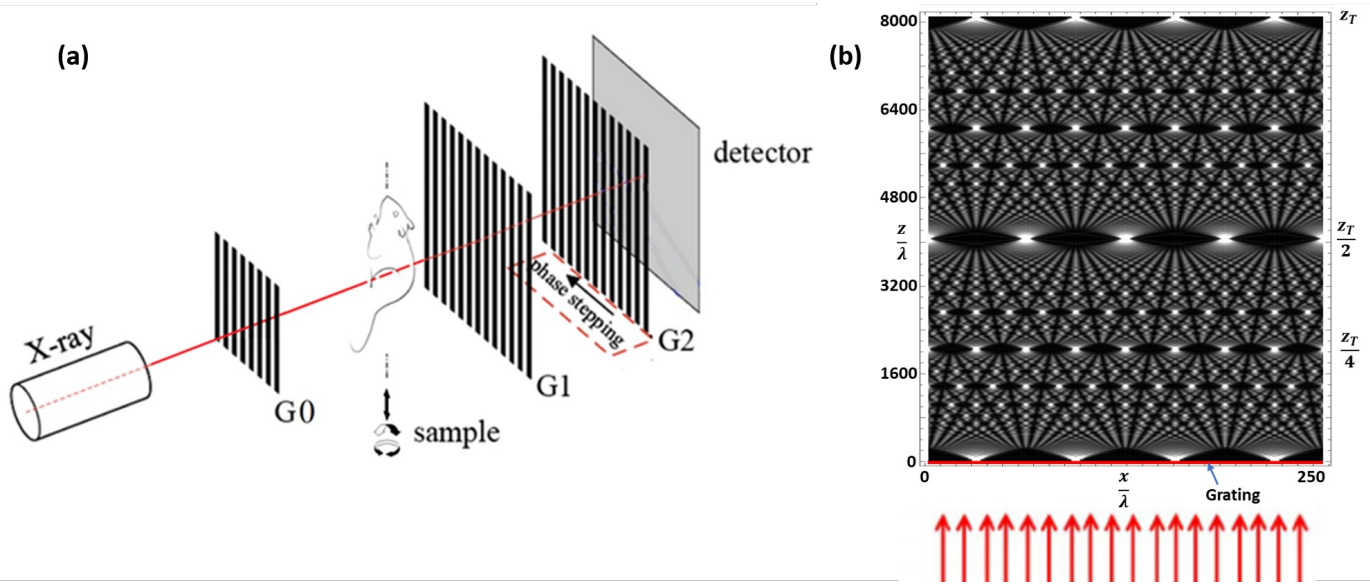
1. INTRODUCTION

To take advantage of the full potential of X-ray CT, there is a need for imaging systems that measure the full extent of the physics (attenuation, differential phase-shift, small angle scatter) involved in the interaction of X-rays with soft tissues. In a recent review it was demonstrated that interferometry-based X-ray imaging can provide excellent soft-tissue contrast of phase and directional small angle scatter information in addition, attenuation properties of tissues common in present day X-ray CT.[1] We propose to design such imaging systems using refractive bi-prisms[2,3] with optimum material and geometric parameters to provide fine spatial fringe modulation with high intensity, and to develop novel X-ray tubes that eliminate the need for mechanical phase stepping.

1.A. Difference between grating and bi-prism interferometry

There are a variety of X-ray phase contrast techniques all of which are based on the observation of interference patterns between deviated and un-deviated rays. Some approaches generate a Talbot-Lau interference pattern shown in Fig. 1 using a grating. This produces a replication of the grating via overlapping interference fringe patterns at regular distances away from the source. By placing the detector at the particular distance where the signal of the intensity is amplified and using methods to measure phase shifts in the interference fringes one is able to separate X-ray attenuation, phase, and scatter of the sample being imaged by comparing the observed pattern with and without the sample. In Fig. 1 for a plane wave passing through a grating, we see different fringe patterns mimicking the source images at regular distances from the source. We will show for the bi-prism interferometer that the amplified fringe patterns are not found at periodic longitudinal distances. Moreover, we will show that the visibility of many, but not all, of the fringe patterns is diminished by the increased numbers of bi-prisms.
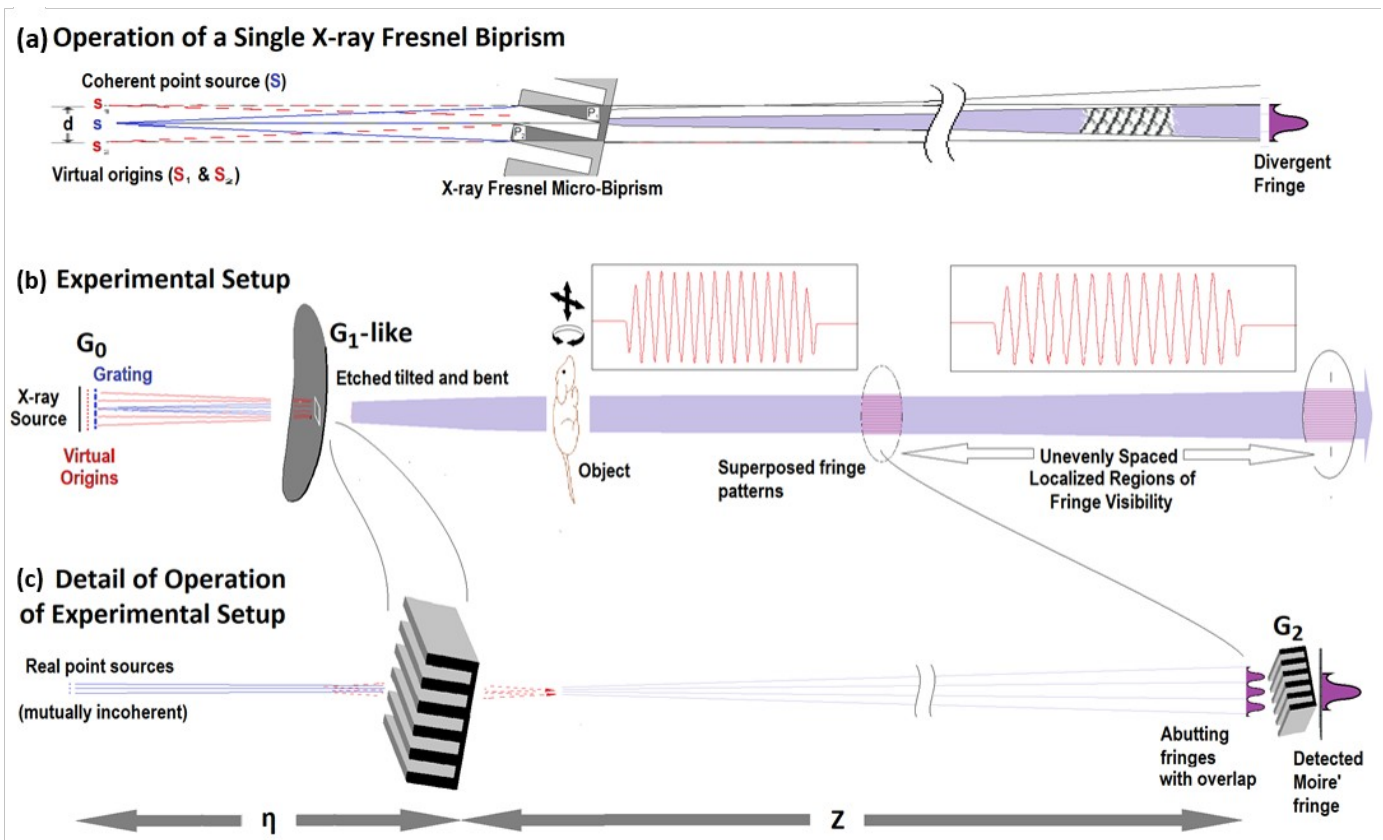
Fig. 1. (a) Schematic diagram of an X-ray grating interferometry system. (b) Talbot-Lau carpet. Illuminating plane wave passes through a grating producing a fringe pattern with replicating amplified fringe patterns at regular distances from the sources produced by the grating. At $Z_T/2$ there is a secondary Talbot image and at Z_T a replication of the original Talbot image that emerged from the grating. At $Z_T/4$ there is a double frequency fractional image and increased frequency of images at less fractional distances. (Modified from Wikipedia: https://en.wikipedia.org/wiki/Talbot_effect.)

In our lab, we are investigating a novel X-ray interferometer (Fig. 2) wherein an array of Fresnel bi-prisms produces interference fringes with X-rays from a source grating (G_0).[4] The system does not have a phase stepping grating (G_2) common in most X-ray phase contrast imaging systems, but our intent is to use hardware, such as a detector/scintillator with small hexagonal elements,[5,6] which acts as a G_2 analyser grating producing a Moiré pattern[7] on the detector. The source grating G_0 forms multiple mutually-incoherent sources of X-ray illumination from a single X-ray source. The multiple mutually-incoherent X-rays sources refract through each element of a bi-prism, thus overlapping as if proceeding from two slightly separated virtual sources of coherent rays (Fig. 3). By selecting bi-prism design parameters of material, angle, number of bi-prisms, period, and bi-prism to X-ray source and to detector distances; the bi-prism array interferometer provides spatially modulated intensity across a wide field as each center fringe thus produced falls in a resonant position at the detector. An X-ray bi-prism material has widely varied refracting power relative to wavelength and thus the separation of the virtual sources also varies with X-ray
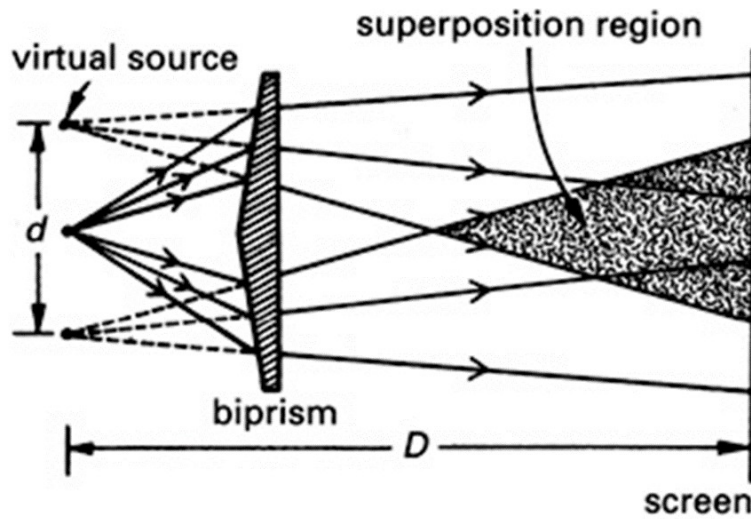
76   wavelength. The setup allows for rotating the sample itself to capture different angular views needed for

77   analysing the X-ray scattering resulting from the orientation of a sample's internal microstructure.

78

79
80   Fig. 2. Schematic diagram of an X-ray bi-prism interferometry system. (a) Operation of a Fresnel X-ray
81   bi-prism, (b) experimental setup with multiple X-ray origins each producing fringes in resonant position,
82   and (c) detail of production of Moiré fringes via a tilted grating G_2 at the detector. Our intention is to
83   eliminate the G_2 granting and instead use only a detector/scintillator with small hexagonal elements to
84   produce the Moiré fringe pattern. (Modified from our earlier publication.[4])

85
86
87

88

Fig. 3. X-ray beam deflection by a bi-prism illustrating the distance d between the two virtual coherent point sources produced by a bi-prism. (Copied from The Fresnel Biprism, David-Alexander Robinson and Jack Denning; Daniel Tanner 08332461; 10th December 2009.)

1.B. Mathematical manipulation of a single exposure of an X-ray phase contrast interferometer

To reduce the acquisition time and dose, mathematical data processing methods have been developed to extract the data from a single exposure. One method[8] "reverse projection" processing is based on manipulation of the phase relation between different X-ray projections and uses tomography to reconstruct the absorption coefficient and refractive index by filtered backprojection of sampled projections. Another method using a single lead grid,[9,10] relies on Fourier analysis of spatial harmonics to obtain absorption, differential phase contrast, and diffraction images, all with a single exposure. The method assumes that refraction and diffraction in the imaged object is manifested as position shifts and amplitude attenuation of the fringes, respectively. In an additional method,[11] the scan of the phase-stepping grating is combined with the rotation of the sample so that a single detector frame per projection angle is obtained, yielding images corresponding to all three contrast modalities. Most single shot methods produce Moiré fringe patterns and depends on Fourier analysis to extract the attenuation, phase, and small angle scatter.[12-17] In particular one paper[13] used continuous wavelet transforms to extract the phase information from Moiré interferograms. In another paper,[16] Moiré fringe patterns are produced by positioning a two-dimensional checkerboard grating at the first Talbot position beyond the object being imaged. Differential phase-contrast and absorption

6

107   images are obtained by Fourier analysis of the Moiré fringe patterns. In two other papers,[15,17] in addition to

108   the source grating (G_0), the phase grating (G_1) and the analyzer grating (G_2) are designed and manipulated

109   to produce a Moiré pattern. In the future, our goal is to develop an imaging system that produces a Moiré

110   pattern without a G_2 grating.

111

112   **1. D. Applications of bi-prism interferometry**

113   Our bi-prism setup is the first to explore X-ray phase contrast bi-prism interferometry in a laboratory

114   setup. The bi-prism is a different approach from gratings to produce refracted waves for extracting the

115   properties of X-rays. Its fringe pattern is divergent in most setups. Bi-prisms have had many applications in

116   the optical regime.[2] Most of the investigations in X-ray bi-prism applications has been using hard X-rays

117   generated in synchrotrons.[3,18-21] However, it has also found application to illustrate the wave-particle

118   behaviour in the single-photon regime.[22,23] Bi-prisms have also been used in interference electron

119   microscopy.[24]

120   **Outline of paper.** In the following we develop analytical expressions for the irradiance distribution of an

121   array of bi-prisms. Using the expressions, we demonstrate the non-periodic pattern characteristic of a bi-

122   prism interferometry system. We also evaluate results of various design parameters for a bi-prims

123   interferometry system. We provide results for 17.5 keV X-rays with silicon and a plastic/epoxy photoresist

124   material (SU-8) demonstrating irradiance distributions for different number of point sources, point source

125   separations, and bi-prism angles. We then investigate the possibility of a nickel bi-prism array for 59 keV

126   that one might consider in the design of a high energy X-ray CT scanner. The results are followed by a

127   discussion of the potential merits of bi-prism interferometry.

2. MATERIALS AND METHODS

2.A. X-ray bi-prism interferometry system

In this paper, we propose a modified X-ray interferometer (Fig. 2) wherein the phase grating (G_1) is replaced with an array of Fresnel micro-bi-prisms. A novel design for the source grating (G_0) is also provided and the analyzer grating (G_2) might be eliminated, though in our present analysis we use a rotated grating (G_2) to produce a Moiré pattern. The Fresnel bi-prism produces high-contrast fringes with spatially incoherent X-ray illumination. The bi-prism array is composed of 7,000 sets of two counter-positioned refractive prisms illuminated with multiple sources. X-rays refracting through each prism element overlap and form divergent (magnified) interference fringes on a distant detector. A further advantage when using polychromatic radiation is that the central fringe produced by a bi-prism is always a "white light" fringe.[25]
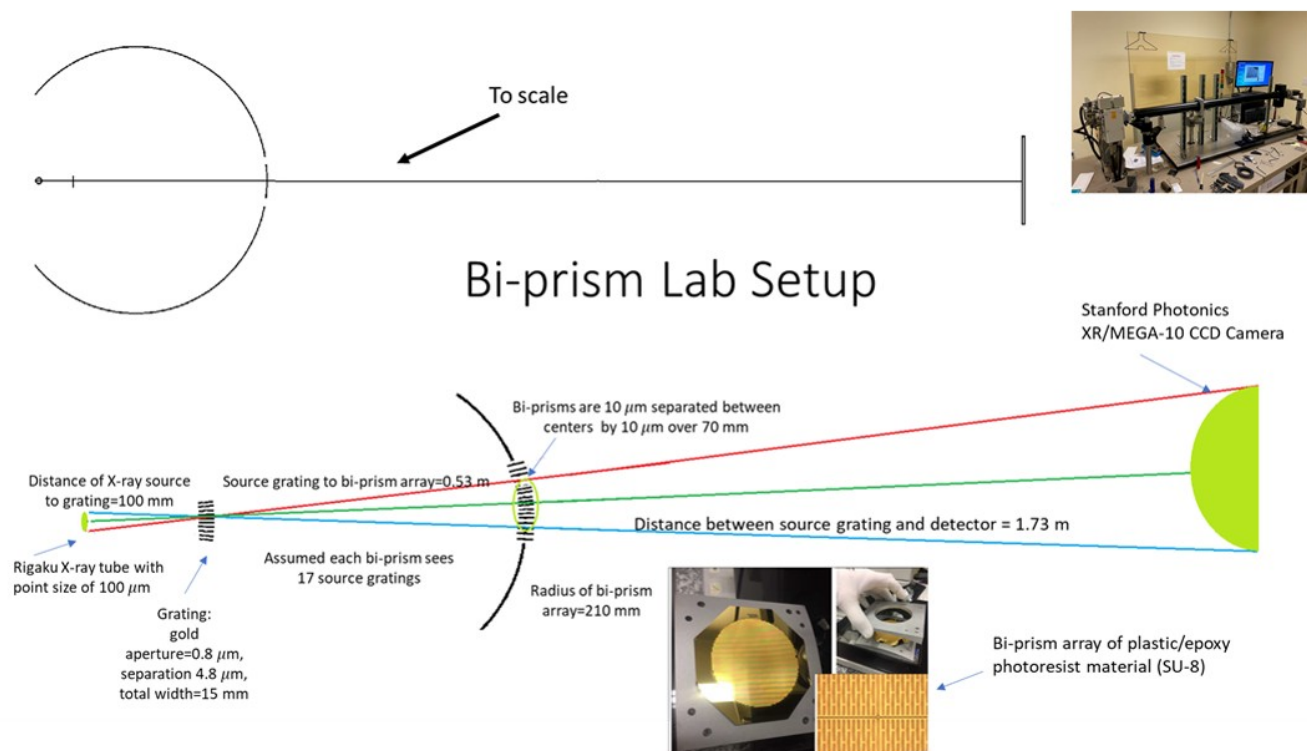
Fig. 4. Lab setup of the bi-prism interferometry system at UCSF. The bi-prism interferometry system includes a molybdenum-target X-ray tube operating at 35 kVp with predominate energy of the 17.5 keV characteristic line (designed energy/wavelength). Shown also is a gold source grating with 0.8 μm apertures separated by 4.8 μm, a bi-prism array made of plastic/epoxy photoresist material (SU-8), and a Stanford Photonics iCCD camera.

145   Our laboratory bi-prism interferometry system (Fig.4) includes a Rigaku X-ray tube (Rigaku Corp.,

146   Akishima-shi, Tokyo, Japan) operating at 17.5 keV with a point-size of 100 μm and a 15 mm wide gold

147   source grating with 0.8 μm apertures separated by 4.8 μm. The bi-prism array consisting of multiple 10 μm

148   bi-prisms with centers separated by 10 μm is curved with radius of 210 mm (We assumed flat in our

149   numerical calculations.), is located 0.53 m from the source grating, and is a plastic/epoxy photoresist

150   material (SU-8) with refraction index decrement of $\delta = 8.7 \times 10^{-7}$. A gold source grating with 0.8 μm

151   apertures separated by 4.8 μm provides multiple point sources to the bi-prisms of coherent sources of X-

152   rays, which are each mutually incoherent. The X-ray tube source size determines the number of point

153   source apertures that illuminate a single bi-prism. We assume that each point source aperture will radiate 17

154   separate bi-prisms. The detector is a Stanford Photonics CCD camera and is located 1.73 m from the source

155   grating.

156   Our work is aimed at imaging small objects at energies of 17.5 keV; however, our X-ray source to detector

157   distance is appropriate for a human size X-ray CT scanner. The equations developed in the following section

158   provide parameters that one can change to design a bi-prism interferometry system at higher X-ray energies.

159

160   **2.B. Analytical expression for the irradiance distribution pattern**

161   In the following section, we develop analytical equations for the irradiance distribution pattern for our bi-

162   prism interferometry system. We use these equations to plot the distribution of fringes for different

163   parameters of a bi-prism interferometry system.

164   Assuming an X-ray beam proceeding from a spatially incoherent planar source with wavelength λ

165   illuminates a thin bi-prism (Fig. 3), we write the irradiance distribution I of X-ray sources on an arbitrary

166   plane placed at a distance z beyond the bi-prism as[2]

167

$$I(\vec{x}, z; \eta) = \frac{\eta^2}{z^2} I_S\left(\frac{-\eta \vec{x}}{z}\right) \otimes_2 I_0(\vec{x}, z; \eta), \tag{1}$$

168   where η is the distance between the source and the bi-prism, z is the distance between the bi-prism and the

169   imaging plane, $\otimes_2$ is the 2D convolution performed over the transverse coordinates $\vec{x}=(x,y)$, I_S is the

170   irradiance distribution of the planar source, I_0 is the irradiance distribution of the Fresnel bi-prism, and I is

171   the irradiance distribution at the observation plane.

172   For a spherical wavefront proceeding from a point source illuminating a Fresnel bi-prism, the exiting

173   wavefront produces an interference pattern I_0 beyond the Fresnel bi-prism whose irradiance distribution is

174
$$I_0(\vec{x},z;\eta)=1+\cos\left(\frac{2\pi x}{p}\right),$$

175   where $p=\lambda(\eta+z)/(2\eta\tan a)$ is the period of the interference pattern, $a=\delta\tan\chi$ is the angle of the beam

176   deflection,[3] δ is the refraction index decrement, and χ is the angle of the bi-prism shown in Fig. 5. Here the

177   expression for the period of the interference pattern for X-rays differ from the expression for light:[2]
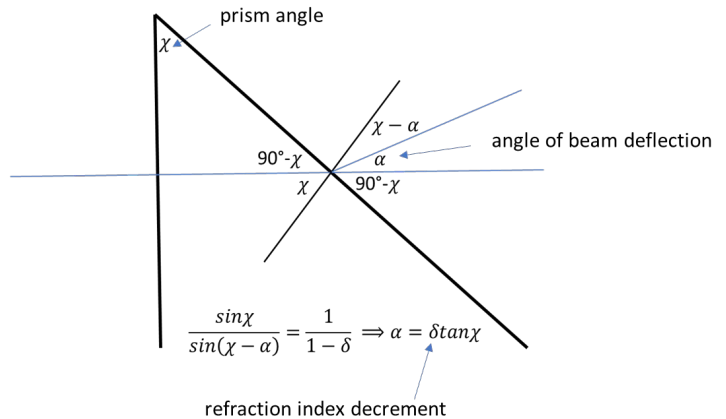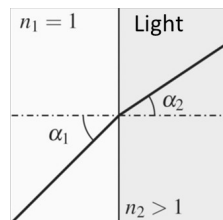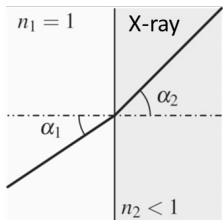
178   $p=\lambda(\eta+z)/(2(n-1)\eta\theta)$, where n is the index of refraction and θ is the refringence angle of the bi-prism.

179   Note that light rays refract toward the normal to the material interface and X-rays refract away from the

180   normal (Fig. 5).
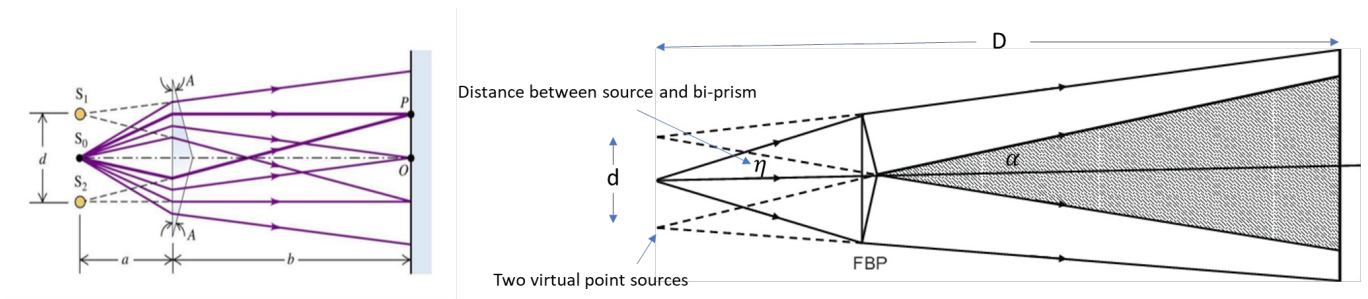
181

10

182   Fig. 5. X-ray beam deflection by bi-prism. Here is given the expression for the angle α of the beam
183   deflection and the distance d between the two virtual coherent point sources produced by a bi-prism. δ is
184   the refraction index decrement. Notice the difference in refraction between X-rays and light. (Modified from
185   Chegg Study, www.x-ray-optics.de, and researchgate.net)
186   Of special interest is a source composed by an array of N_s mutually incoherent point sources with the

187   same irradiance, I_P, and arranged equidistant perpendicular to the bi-prism edge and distributed

188   symmetrically to the optical axis. In a realistic experimental situation, the width $\varDelta$ of the sources along the

189   x- and y-direction would not be infinitesimal. In that case, the irradiance distribution of each source can be

190   written as the convolution between a delta function and a rectangular function of width $\varDelta$:

191    $h(x,y)=I_P\delta(x,y)*\Pi\left(\dfrac{x}{\varDelta},\dfrac{y}{\varDelta}\right).$

192   (Note: Here $*$ refers to the 2D convolution.) If the point sources are located with x-coordintes

193    $x_i=\left(\dfrac{N_s+1}{2}-i\right)x_0, i=1,\ldots\ldots, N_s,$

194   where x_0 is the separation between neighbor point sources, then from Eq. (1) the irradiance distributions of

195   each point source is

196    $g(x,y,z;\eta,x_i)=h(\dfrac{-\eta x}{z}-x_i,\dfrac{-\eta y}{z})*I_0(x,y,z;\eta)=h\left(\dfrac{-\eta x}{z}-x_i,\dfrac{-\eta y}{z}\right)*\left[1+\cos\left(\dfrac{2\pi x}{p}\right)\right],$

197   where $-z/\eta$ is the magnification factor between the source and observation plane. The irradiance

198   distribution of all the sources is therefore the summation of the distribution of source irradiances

199    $I(\vec{x},z;\eta)=\dfrac{\eta^2}{z^2}\displaystyle\sum_{i=1}^{N_s}g(x,y,z;\eta,x_i).$

200   Using Mathematica (Wolfram Research, Champaign, Illinois), we come up with the following analytical

201   expression for the irradiance distribution pattern for $N_b=1$ (one bi-prism):[4]

202    $I_{N_b=1}(x,z;\eta)=\begin{cases} I_p\left(\varDelta^2+\dfrac{p\,\eta\varDelta}{\pi z}\cos\left[\dfrac{2\pi x}{p}\right]\sin\left[\dfrac{\pi z\,\varDelta}{p\eta}\right]\right) & if\ N_s=1 \\[2ex] I_p\left(N_s\varDelta^2+\dfrac{p\,\eta\varDelta}{\pi z}\cos\left[\dfrac{2\pi x}{p}\right]\sin\left[\dfrac{\pi z\,\varDelta}{p\eta}\right]\csc\left[\dfrac{\pi x_0 z}{p\eta}\right]\sin\left[\dfrac{\pi N_s x_0 z}{p\eta}\right]\right) & if\ N_s>1 \end{cases},$ (2)

203   where

11

204
$$p = \lambda(\eta + z)/(2\eta\tan\alpha) = \lambda(\eta + z)/[2\eta\tan(\delta\tan\chi)]$$

205 is the period of the interference pattern. Notice that the expression is given only as a function of the x-

206 coordinate, assuming the irradiation distribution in y is minimal.

207   Equation (2) gives an expression for one bi-prism with one and multiple point sources. To obtain an

208 expression for multiple bi-prisms, we used Mathematica to sum the irradiance distribution of N_b shifted bi-

209 prisms separated by x_b using the expression

210
$$I(x, z; \eta) = \sum_{j=1}^{N_b} I_{N_b=1}\left[\left((N_b + 1)/2 - j\right)x_b\right] \quad,$$

211 to obtain the following expression for multiple bi-prisms and multiple sources:

212
$$I(x, z; \eta) = I_p\left[N_b N_s \Delta^2 + \frac{p\,\eta\Delta}{\pi z}\cos\left(\frac{2\pi x}{p}\right)\csc\left(\frac{\pi x_0 z}{p\eta}\right)\csc\left(\frac{\pi x_b}{p}\right)\sin\left(\frac{N_s \pi x_0 z}{p\eta}\right)\sin\left(\frac{N_b \pi x_b}{p}\right)\sin\left(\frac{\pi z \Delta}{p\eta}\right)\right].$$

213   (3)

214

3. RESULTS

Mathematica was used to numerically evaluate Eq. (2) to obtain fringe patterns behind a bi-prism for incoherent X-ray point sources located at $\eta=0.4$ m in front of the bi-prism (see Fig. 6). For the calculation we set $\lambda=7.1\times10^{-11}$m, $I_p=1/\Delta^2$, $\Delta=7.00\times10^{-7}$, and $\alpha=\delta\tan(\chi)$, where $\delta=1.57\times10^{-6}$. Using these parameters, calculations were made for 25-point sources with a bi-prism angle of $\chi=82°$. The scale increases in proportion to the number of point sources.[4] Non-periodic visibility is seen in Fig. 6. This is characteristic of a fringe pattern for a bi-prism and differs from the periodic pattern of the well-known Talbot–Lau interferometer with gratings in Fig. 1.
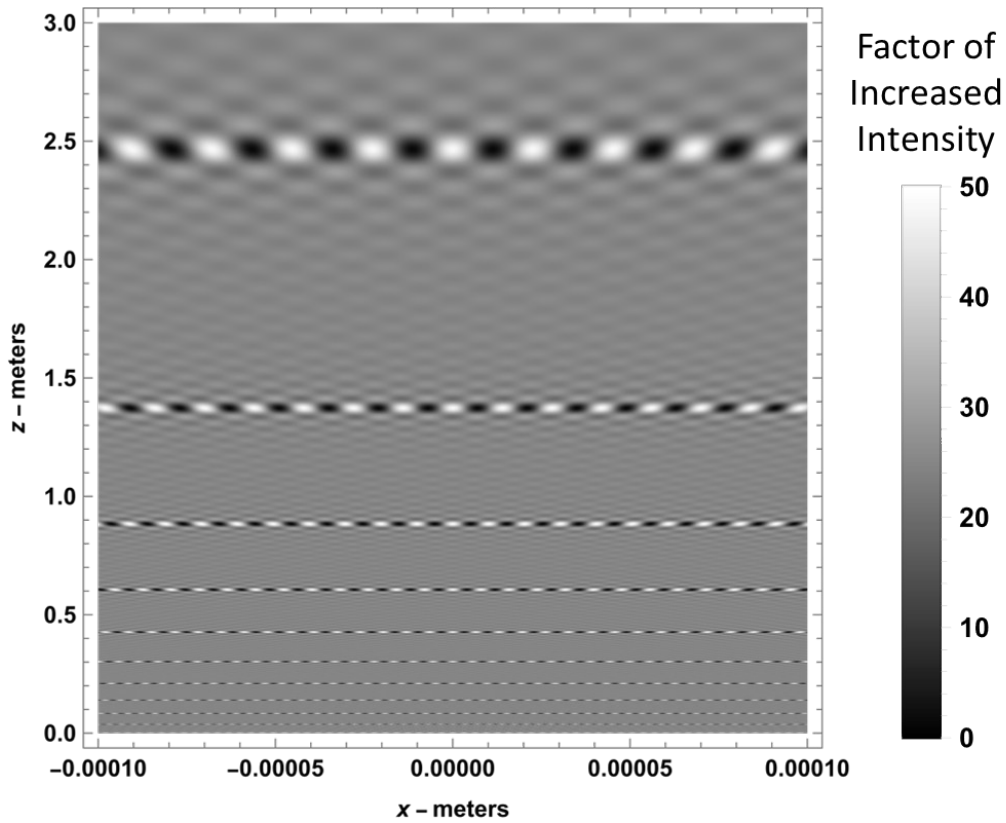
Fig. 6. Density plot of a fringe pattern for 25-point sources with 1 bi-prism. The amplification of the interference pattern is repeated at non-periodic distances away from the plane of the bi-prism. For the calculation we set $\lambda=7.1\times10^{-11}$ m (17.5 keV), $I_p=1/\Delta^2$, $\Delta=7.00\times10^{-7}$ m, $\alpha=\delta\tan(\chi)$, $\delta=1.58\times10^{-6}$ (silicon), $\chi=82°$, $\eta=0.4$ m, and $x_0=36.7\,\mu$m. This figure is modified with new parameters from that of our previous publication.[4]

13

230   Notice that in our calculations using Eq. (2) we set the irradiance I_p of each point source to $1/\Delta^2$. One

231   might want to consider this to be a flux of 1 photon per Δ^2. Then the resultant intensity in Eq. 2 is a total

232   number of photons. However, since we do not know the photon flux of the source, we interpret the result of

233   Eq. (2) as a relative measure or factor of increase in intensity. Keep in mind that our equations represent

234   refraction and do not include attenuation.

235   Mathematica was also used to numerically evaluate Eq. (3) to obtain a density plot in Fig. 7 of a fringe

236   pattern behind one bi-prism with 17-point sources for set of parameters used in our laboratory setup that

237   differed from those in Fig. 6.
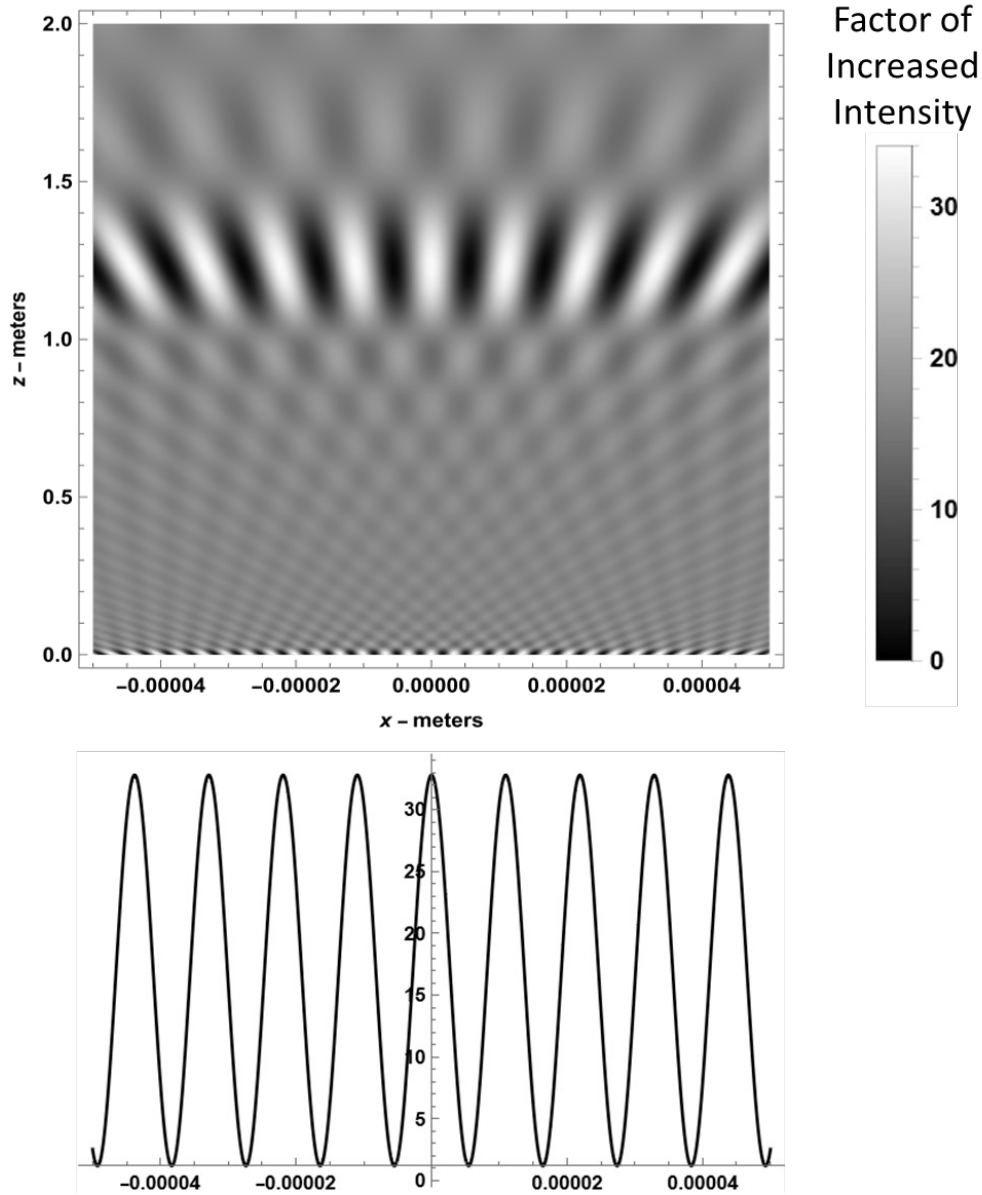
Fig. 7. Density plot of a fringe pattern for 17-point sources with 1 bi-prism for a different set of parameters than those in Fig. 6. For the calculation we set $\lambda = 7.1 \times 10^{-11}$ m (17.5 keV), $I_p = 1/\Delta^2$, $\Delta = 8.00 \times 10^{-7}$ m, $\alpha = \delta \tan(\chi)$, $\delta = 8.7 \times 10^{-7}$ [plastic/epoxy photoresist material (SU-8)], $\chi = 85.3°$, $\eta = 0.53$ m, and $x_0 = 4.8 \, \mu$m, $x_b = 10 \, \mu$m. There is a fringe separation of 1.09×10^{-5} m at $z = ¿1.2$ m.

If we change the source separation in Fig. 7 from $x_0 = 4.8 \, \mu$m to $x_0 = 36.7 \, \mu$m, we see a very different

fringe pattern in Fig. 8. This demonstrates that the fringe pattern is sensitive to the distance x_0 between the
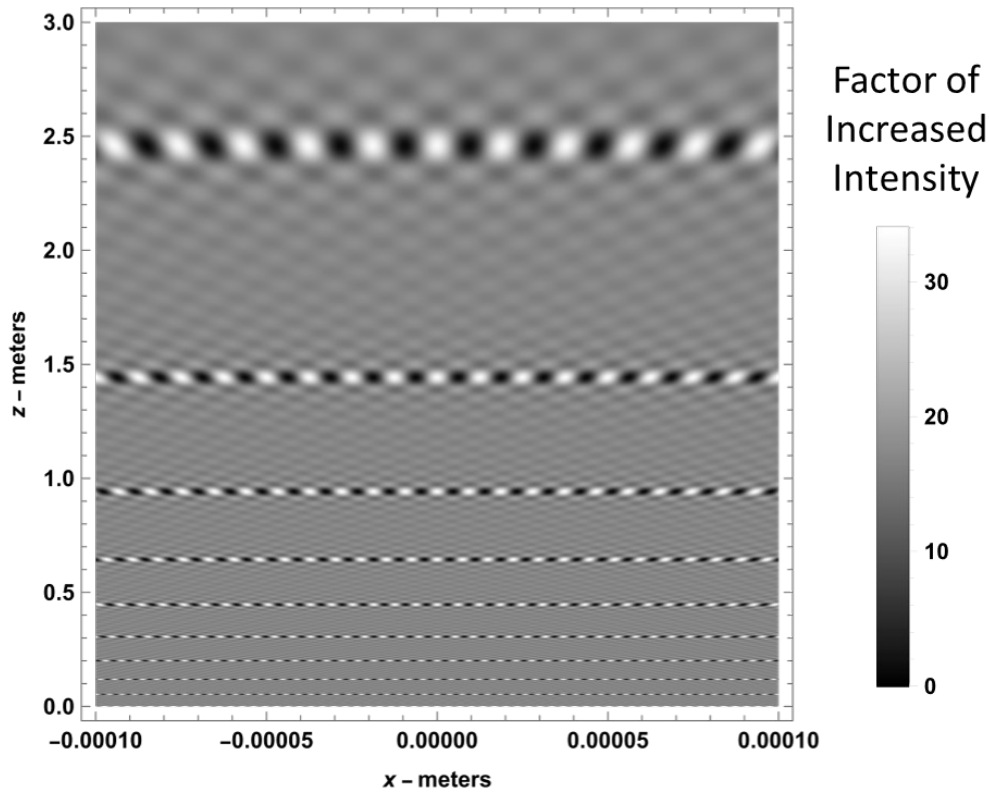
point sources.

248

249   Fig. 8. Density plot of a fringe pattern for 17-point sources with 1 bi-prism for the same set of parameters
250   as those in Fig. 7, except x_0 was changed from $x_0=4.8\,\mu$m to $x_0=36.7\,\mu$m For the calculation:
251    $\lambda=7.1\times10^{-11}$m (17.5 keV), $I_p=1/\Delta^2$, $\Delta=8.00\times10^{-7}$ m, $a=\delta\tan(\chi)$, $\delta=8.7\times10^{-7}$ [plastic/epoxy
252   photoresist material (SU-8)],$\chi=85.3\,°$, $\eta=0.53$ m, and $x_0=36.7\,\mu$m, $x_b=10\,\mu$m.
253

254   The fringe pattern is sensitive to the bi-prism material, the bi-prism angle χ, and the distance x_0 between

255   the point sources. In Fig. 6 the fringe pattern corresponds to silicon ($\delta=1.58\times10^{-6}$) with parameters

256    $\chi=82\,°$, $\eta=0.4$ m, $x_0=36.7\,\mu$m, and $\Delta=7.00\times10^{-7}$ m; whereas, in Fig. 7 the fringe pattern corresponds to

257   SU-8 material ($\delta=8.7\times10^{-7}$) used in our laboratory setup with parameters $\chi=85.3\,°$, $\eta=0.53$ m, $x_0=4.8\,\mu$

258   m, and $\Delta=8.00\times10^{-7}$. Since the refractive index decrement of SU-8 is less than silicon, thus decreasing

259   the angle of deflection ($a=\delta tan\chi$); in our design we increased the angle of each bi-prism to $\chi=85.3\,°$.

260   Probably the significant increase in the number of non-periodic fringes in Fig. 8 is due to changing the

261   source separation from $x_0=4.8\,\mu$m to $x_0=36.7\,\mu$m.

262   The visibility, $(I_{max}-I_{min})/(I_{max}+I_{min})$, was calculated for a few examples by finding the minimum and

263   maximum intensity for ±5 μm in x about the maximum central fringe. If we use 17-point sources with one

16

264 bi-prism, as in Fig. 8, we obtain a visibility of 0.93. If the point source separation is change from 36.7 μm

265 to 4.8 μm the visibility is improved to 0.95. If for the same point source separation of 36.7 μm, the point

266 source size Δ is changed from 8×10^{-7} to 4×10^{-7}, the visibility is improved even more to 0.98. These trends

267 in the visibility calculations are as one would expect; however, are higher than one would expect in a

268 laboratory X-ray phase contrast interferometer. The work of Isakovic et al.[19] provided bi-prism

269 measurements performed at the Brookhaven National Laboratory synchrotron where a single bi-prism was

270 evaluated in an X-ray beam of 9.5 keV. Their data showed a difference in fringe visibility in the vertical

271 and the horizontal axis, with a maximum fringe visibility in the vertical above 0.9 and approximately 0.6 in

272 the horizontal axis. From this, they calculated an effective asymmetric source of their beamline as a vertical

273 source of 10 ± 5 μm and a horizontal source of 130 ± 20 μm. From generally known parameters, the

274 transverse coherence length of that beamline would be ~160 μm in the vertical and ~12.3 μm in the

275 horizontal. In the simulation of our laboratory setup, we use an array of 0.8 - μm sources at 0.53-meters in

276 front of an array of bi-prisms. At 17.5 KeV, the transverse coherence length of the operable axis is 11.8 -

277 μm and one would expect to produce one central fringe per each source/bi-prism pair. Of course, our

278 proposed setup is an array of bi-prisms with a source grating as an array of small sources; thus, the detector

279 records many such fringes each falling in resonant positions.

280 Again, using Mathematica to numerically evaluate Eq. (3), we obtained a fringe pattern behind 101 bi-

281 prisms for 17-point sources. Notice in Fig. 7 that for a single bi-prism the maximum intensity is at

282 approximately $z=¿1.2$ m, whereas, in Fig. 9 for 101 bi-prisms, the maximum intensity appears to be at $z=¿$

283 1.05 m. Increasing the number of bi-prisms increases the fringe intensity and shifts the maximum intensity

284 toward the sources while bringing the maximum fringe intensity more in focus and greatly reducing fringe

285 intensity in other regions.

286
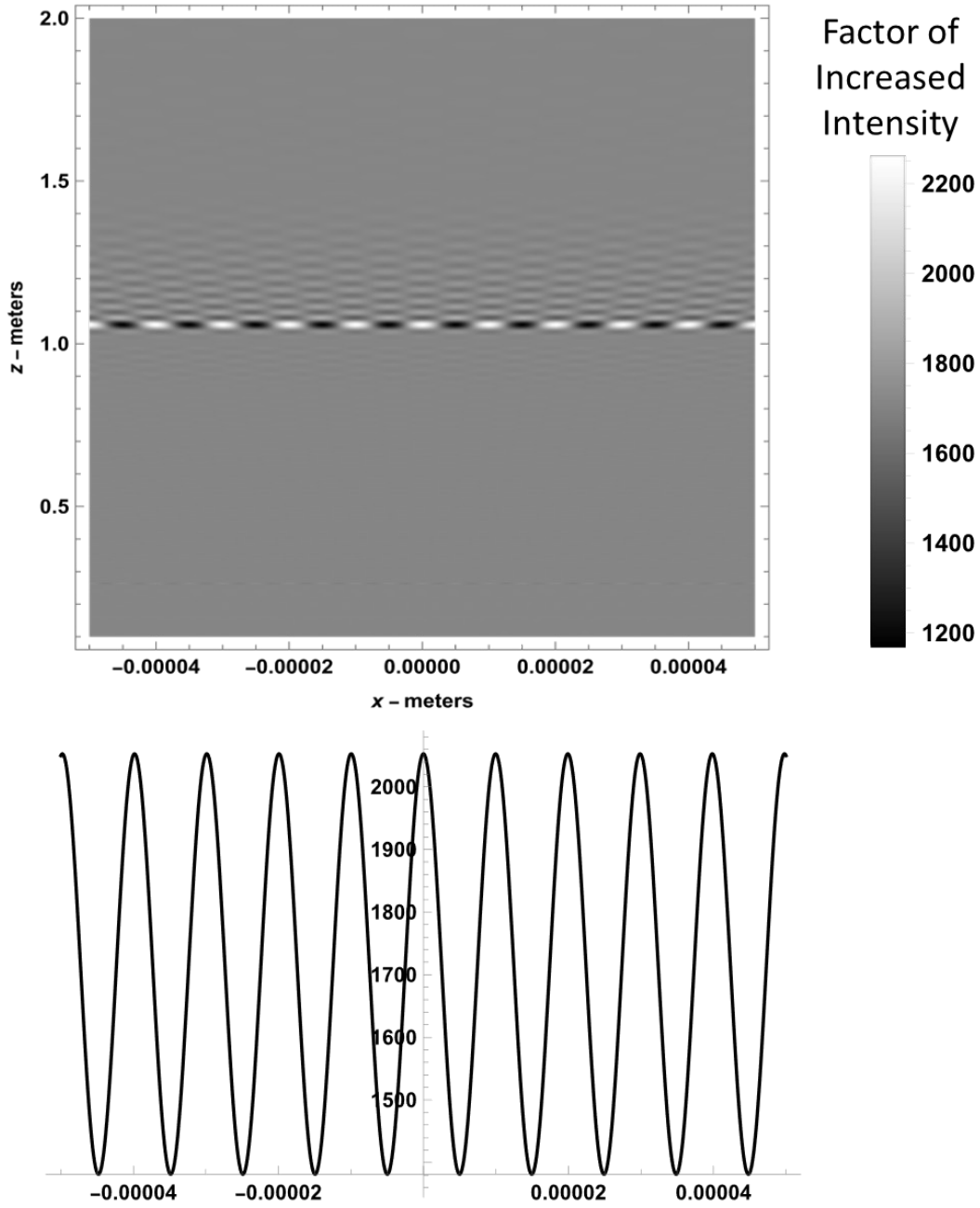
Fig. 9. Density plot of a fringe pattern for 17-point sources with 101 bi-prism for the same set of parameters as in Fig. 7. For the calculation we set $\lambda = 7.1 \times 10^{-11}$m (17.5 keV), $I_p = 1/\Delta^2$, $\Delta = 8.00 \times 10^{-7}$ m, $a = \delta \tan(\chi)$, $\delta = 8.7 \times 10^{-7}$[plastic/epoxy photoresist material (SU-8)], $\chi = 85.3°$, $\eta = 0.53$ m, and $x_0 = 4.8\,\mu$ m, $x_b = 10\,\mu$m. There is a fringe separation of 1.00×10^{-5} m at $z = ¿1.05$ m.

The equations developed in this section provide plots of the non-periodic fringe pattern, the intensity of

the maximum fringe intensity, and the fringe separation at the maximum fringe intensity for our laboratory

bi-prism design. Equation (3) was used to compare different possible designs of a bi-prism interferometry

18

297   system for parameters given in Table 1. Designs were compared between a bi-prism material of our

298   present lab setup of plastic/epoxy photoresist material (SU-8) and silicon at 17.5 keV. The refractive index

299   decrement for SU-8 was not listed in the CXRO online calculator,[27] but is a similar plastic to PMMA. The

300   paper of Mamyrbayev et al.[26] states on page 7 that the refractive index of SU-8 is 9.23×10^{-7} at 17 keV,

301   which is the value CXRO calculates for PMMA at 17 keV. The evaluations in our paper were performed

302   for 17.5 keV, thus we used the value of $\delta = 8.7 \times 10^{-7}$ for SU-8 at 17.5 keV which is the value for PMMA

303   at 17.5 keV in the CXRO online calculator.[27]

304   By selecting different bi-prism materials, one can design a system that would be appropriate for an X-ray

305   CT system with higher X-ray source energy than the 17.5 keV used here in our validations. In our

306   demonstrations here, we have attempted to keep the distance between the X-ray source and detector with

307   reasonable real world X-ray imaging applications. By modifying the bi-prism material and angle of the bi-

308   prism one maintains reasonable X-ray source to detector distances. Silicon and our laboratory SU-8

309   material are not ideal for a higher energy of 59 keV. A better material would be nickel. A value of

310     $\delta = 5.06 \times 10^{-7}$ was obtained for nickel at 59 keV from the X-Ray Optics Calculator.[28] As one sees from

311   Table 1, the fringe separation decreased by a factor of approximately 3. The angle of the bi-prism is also a

312   function of the material with silicon requiring a smaller angle to bring the detector distance close to that of

313   our SU-8 material, whereas in Table 1 we see that an increased angle of 87°is required for nickel.

314

315

316

317

318
319
320   Table 1. Equation (3) was used to calculate the fringe separation and the fringe intensity for our laboratory
321   bi-prism SU-8 material and compared to silicon at 17.5 keV. The fringe separation was nearly $10\,\mu m$ for
322   our laboratory setup and would be the same for the designated parameters for a bi-prism material of silicon.

323 The same equation was used to design a bi-prism nickel interferometry system at 59 keV. The distances
324 between the bi-prisms and the selected detector positions were determined by observing the density plots
325 like the one in Fig. 9.
326
327

	Design 1 (Fig. 6)	Design 2	Design 3	Design 4 (Fig. 9)	Design 5
Bi-prism material	Silicon	plastic/epoxy photoresist (SU-8)	Silicon	plastic/epoxy photoresist (SU-8)	Nickel
Energy	17.5 keV	17.5 keV	17.5 keV	17.5 keV	59 keV
Wave length λ	7.1×10^{-11} m	7.1×10^{-11} m	7.1×10^{-11} m	7.1×10^{-11} m	2.14×10^{-11}
Refractive index decrement δ	1.58×10^{-6} *	8.7×10^{-7} **	1.58×10^{-6} *	8.7×10^{-7} *	5.06×10^{-7} +
Bi-prism angle χ	82°	85°	82°	85.3°	87°
Angle of deflection α	11.2×10^{-6}	9.9×10^{-6}	11.2×10^{-6}	10.63×10^{-6}	9.66×10^{-6}
Bi-prism separation x_b	---	---	10μm	10μm	3.65μm
Number of bi-prisms N_b	1	1	101	101	101
Number of X-ray sources N_s	25	25	17	17	17
Source size Δ	7.00×10^{-7} m	7.00×10^{-7} m	8.00×10^{-7} m	8.00×10^{-7} m	8.00×10^{-7} m
Pt. source separation x_0	36.7μm	36.7μm	$4.8 \mu m$	$4.8 \mu m$	$6 \mu m$
Distance between source and bi-prism η	0.4 m	0.4 m	0.53 m	0.53 m	0.51 m
Distance between bi-prism and detector z	1.38 m	1.4 m	1.14 m	1.05 m	1.19 m
Fringe separation	14.1×10^{-6} m	16.1×10^{-6} m	10.0×10^{-6} m	10.0×10^{-6} m	3.69×10^{-6} m
Factor of increase in fringe intensity	46.2	48.6	2176	2052	1733

328
329   * CXRO online calculator[26]
330   **SU-8 is similar to PMMA in CXRO online calculator[26,27]
331   + X-Ray Optics Calculator (http://purple.iptm.ru/xcalc/xcalc_mysql/ref_index.php)[28]
332
333
334
335   In a previous publication[4] we showed that the distance to the maximum fringe pattern is sensitive to

336   small changes in the angle of the bi-prism. To study this, one can look at a simple case of one point source

337   and one bi-prism. We first write the intensity in Eq. (1) as a function of the angle of the bi-prism χ:

338    $Intensity[\chi, x, z] = ¿$

339    $$Ip\left(\varDelta^2 + \frac{\varDelta}{\pi z}((\eta+z)*\lambda)/(2\tan[\delta\tan(\chi)])\right)\cos\left\{\frac{4\pi x\eta\tan[\delta\tan(\chi)]}{(\eta+z)*\lambda\,¿}¿\right\}\sin\left\{\frac{2\pi z\varDelta\eta\tan[\delta\tan(\chi)]}{(\eta+z)*\lambda\eta}\right\}, \qquad (4)$$

340   where z is the distance between the bi-prism and the fringe pattern and x is the lateral distance on the

341   detector. One can then take the partial derivative of the intensity with respect to the angle to come up with

342   the expression:

343    $$\frac{\partial\,Intensity(\chi, x, z)}{\partial\chi} = \frac{-1}{2\pi z}Ip\,\delta\varDelta\,csc[\delta\tan(\chi)]\sec(\chi)^2\,¿$$

344   Using this expression, we obtain plots of the sensitivity of the Intensity as a function of the angle of the

345   bi-prism (Fig. 10). One sees that the derivative of the Intensity is fairly flat near the central fringe $x=0$ for

346    $z=1$ m until the angle nears $\pi/2=1.5708$; then it changes rapidly for an energy of 17.5 keV [Fig.10(a)]. For

347   59 keV, the change is more dramatic near $\pi/2$ [Fig.10(b)].
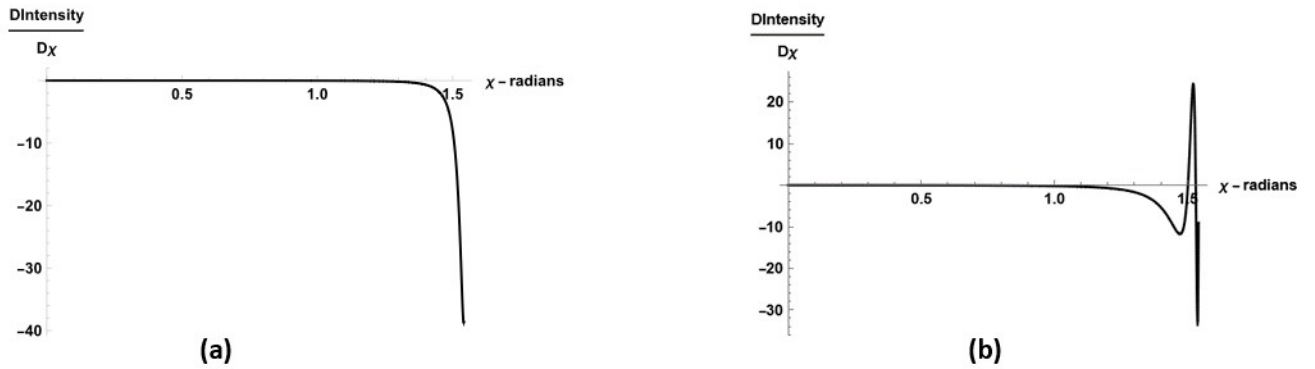
348

349   Fig. 10. Sensitivity as a function of bi-prism angle χ for X-ray source energies of (a) $\lambda=7.1\times10^{-11}$m
350   (17.5 keV) and (b) $\lambda=2.14\times10^{-11}$m (59 keV). For the calculation we set $N_s=1$, $N_b=1$, $I_p=1/\varDelta^2$,
351    $\varDelta=8.00\times10^{-7}$ m, $\delta=8.7\times10^{-7}$ (SU-8), $\eta=0.53$ m, $x=0.000001$ m, and $z=1$ m.
352
353
354   Using Eq. (4) one can study the Intensity variation due to the size of the point source aperture $\varDelta$ and the

355   point source separation x_0. For the parameters in Fig. 9, increasing the point source aperture $\varDelta$ will as

356   shown in Fig. 11 decrease the maximum fringe intensity until the aperture $\varDelta$ approaches that of a point

357   source aperture separation of 4.8 μm with a minimum around $7\mu m$. The Intensity then increases as the

358 apertures continue to overlap the separation between point sources. In Fig. 12 we see that the Intensity will

359 be maximum for point source separations x_0 at factors of $x_b/2 = 5\,\mu$m. This is helpful because we can see

360 that if we change the value of x_b to 5 in Fig. 9, we would have come up with a better factor of increase in

361 intensity of 3238 with a fringe separation of 10.0×10^{-6} m at $z = 1.06$ m.

362
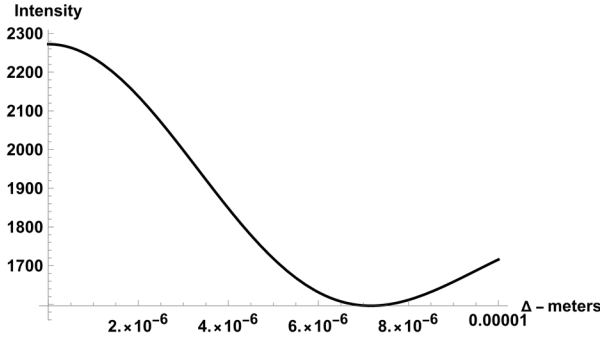
363
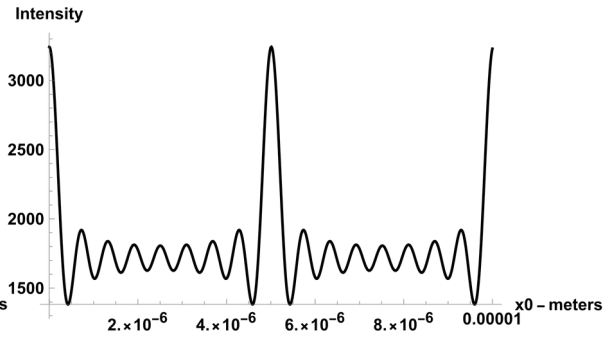
364

365 Fig. 11. Intensity as a function of point source size Δ :
$$Intensity = \frac{13736\,\Delta + \sin(626988\,\Delta)}{8\,\Delta}.$$ For the
calculation we set $N_s = 17$, $N_b = 101$, $I_p = 1/\Delta^2$,
$\delta = 8.7 \times 10^{-7}$ (SU-8), $\chi = 85.32\,°$, $\eta = 0.53$ m,
$x_0 = 4.8\,\mu$m, $x_b = 10\,\mu$m, $x = 0$ m, and $z = 1.06$ m.

Fig. 12. Intensity as a function of separation between point
sources x_0. For the calculation we set $N_s = 17$, $N_b = 101$,
$I_p = 1/\Delta^2$, $\Delta = 8.00 \times 10^{-7}$ m, $\delta = 8.7 \times 10^{-7}$ (SU-8),
$\chi = 85.32\,°$, $\eta = 0.53$ m, $x_b = 10\,\mu$m, $x = 0$ m, and
$z = 1.06$ m.

368

4. DISCUSSION

This study provides expressions for fringe patterns of bi-prism interferometry and demonstrates maximum fringe visibility regions that are not periodic as is common with Talbot–Lau interferometry systems using diffraction gratings. Using the same analytical expressions, we calculate maximum fringe contrast and fringe periods for different X-ray source sizes and separations; and bi-prism design parameters of material, angle, size, number, period, and distances between the source and detector. The expressions are used to design and calibrate our laboratory system so that experiments can be performed that would be appropriate in the design of X-ray CT systems with higher energies and with high-power X-tubes capable of providing phase images almost instantaneously.

4.A. Advantages of a single exposure bi-prism interferometry system

The well-established grating-based method of phase contrast X-ray imaging may yet prove capable of clinical applications. Still, alternative approaches such as the bi-prism method herein discussed holds several possible advantages. For good flux throughput, we have constructed a bi-prism array from the polymer SU8, a popular photoresist useful with LIGA processes. SU8 is a photoactive compound with some high Z components in low percentages. For 17 keV, the data yields 1/e absorption lengths for the polymer of 1825 μm, or a transparency of 97% for our optic design.

A bi-prism works well with polychromatic X-rays, as the fringe period is, in part, determined by the separation of the two virtual sources. This spacing is not fixed, as with a grating or Young's double slit, but rather varies dependent on the refractive index of the prism material relative to X-ray wavelength. Whereas, under polychromatic illumination the design of a grating system should be optimized for a particular frequency of X-rays.[29]

391   Moreover, the fringe period generated from a laboratory bi-prism setup has a relatively large

392   magnification factor of approximately 2.5X. Some publications[30,31] have shown that modifying the standard

393   Talbot-Lau interferometer where by the G_1 grating is placed close to the source can also increase

394   magnification factors similar to those in our bi-prism system. A larger fringe period at the detector could

395   allow using a structured scintillator to record Moiré patterns. A hexagonal structured scintillator (Fig. 13)

396   might aid the fast acquisition of phase contrast data of X-ray attenuation, phase, and small angle scatter.

397   However, there are some challenges with using bi-prisms as well, mostly related to poorer spatial resolution.

398   Even though, bi-prism-based interferometry, or other refractive-optical approaches, hold the potential to

399   revolutionize phase-contrast and dark-field X-ray CT.

400
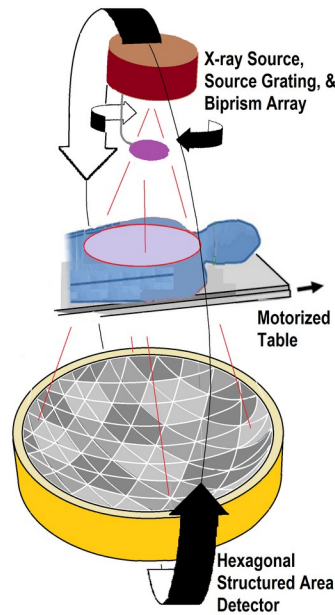
401

402
403   Fig. 13. Proposed cone-beam tensor tomography system. The X-ray source and optics rotate around an
404   axis aligned to the center of an area detector with hexagonally segmented crosstalk-free scintillation
405   elements. The components are mounted on a revolving gantry (for clarity, not shown here). X-ray scatter
406   data is captured for three specific orientations 120º apart for every angular view.
407
408
409   In our previous paper[32] we performed simulations using wave optics to evaluate X-ray phase contrast

410   imaging with grating interferometry using phase stepping and with bi-prism interferometry using single

411   exposure Moiré fringe analysis. Results of reconstructed vector coefficients of small angel scatter showed

412   that bi-prism interferometry with single-exposure Moiré fringe analysis has an increase in noise compared

413   to grating interferometry using phase stepping because of 1/8th the number of projection samples but

414   provides better CNR due to better photon flux with less dose and faster acquisition times.

415

416   *4.A.1. Design of structured scintillators*

417   The implementation of a structured scintillator[5,6] fits well into our design of an X-ray bi-prism

418   interferometry system with single-exposure Moiré fringe analysis because it reduces crosstalk between

419   pixels of our high-resolution large fringe separation. Though the authors of this referenced work aimed

420   their development for grating systems, a structured scintillator is ideal for our bi-prism interferometry

421   system. The structure scintillator consists of filling an array of silicon pores with a thallium-doped cesium

422   iodide [CsI(Tl)] scintillator. The pores act as a mold which are filled with melted CsI(Tl) powder. Before

423   filling, the walls are coated thermally with an oxide layer to provide a wave guide to direct the light and

424   reduce noise between pixels. The design of a structured scintillator prevents crosstalk and allows

425   opportunity for Moiré fringe development when illuminated with spatially modulated X-ray illumination.

426   Moiré patterns occur because of the interaction between the pixelated image sensor and the periodic pore

427   structure of the scintillator. The magnitude of this occurrence depends on the ratio of the respective pitches,

428   the geometries involved and the amount of angular misalignment. The Moiré pattern is ideal for the

429   extraction of dark field scatter by taking the first harmonic of the Fourier transform. The work of

430   Rutishauser et al.[6] showed an increase in fringe visibility at X-ray energies around 60 keV (greater than our

431   simulations of 17.5 keV), leading to an improvement in the quality of the differential phase and dark field

432   data compared to a conventional grating interferometry system.

433

434   *4.A.2. Parameter range for a bi-prism interferometry system*

435   In our laboratory setup, we have been using a Rigaku X-ray tube with molybdenum anode operating at

436   35kVp, where 17.5 keV is the predominate energy with a point-size of 100 μm and a 15 mm wide gold

437   source grating with 0.8 μm apertures separated by 4.8 μm. We assume the multiple point source apertures

438   are the "open windows" of the source grating. These are much smaller than the "closed bars" of a typical

439   source grating and provide to the bi-prism array multiple coherent sources of X-rays, which are each

440   mutually incoherent. There is some reduction in image resolution by using laboratory X-ray tube sources.

441   The actual laboratory X-ray source size is that of a typical X-ray tube and determines the number of "open

442   window" point sources that illuminate a single bi-prism. We assume that each point source aperture will

443   radiate 17 separate bi-prisms. The intensity of the fringe visibility increases with the number of sources and

444   the number of sources seen by each bi-prism. The intensity is maximum if the source separation is a factor

445   of one-half the width of the bi-prism. The intensity also increases with the increase in the angle of the bi-

446   prism. The rate of change of this increase is fairly flat until the angle of the bi-prism nears 90°.

447   Our bi-prism system design, like that proposed by Yaroshenko *et al.*[33] for a grating interferometry

448   system, offers the potential for future X-ray CT application by providing high fringe visibility at shorter

449   propagation distances. They demonstrated that using phase gratings with triangular-shaped structures in an

450   X-ray interferometer can yield high visibilities for significantly shorter propagation distances than

451   conventional gratings with binary structures. This is especially important in the design of human systems

452   where bore sizes are approximately 75-85 cm.

453   Although similar in construction as Yaroshenko *et al*[33] our interferometry methods follow Doblas *et al.*[2] -

454   albeit with X-rays rather than visible light. Where Doblas *et al.* use multiple coherent sources and a single

455   Fresnel bi-prism, we use an array of Fresnel bi-prisms. The full setup yields multiple fringe patterns in

456   resonant superposition with a large field of illumination. Fundamentally, this is a different way to make

457   interference fringes. A single coherent X-ray source can illuminate a single Fresnel bi-prism and produces

458   interference fringes downfield. The fringe patterns produced by our array of bi-prisms are only indirectly

459   related to the array period, but are the direct result of the periodicity of the virtual sources created by the

460   individual bi-prisms in the array. Interference fringes produced by a grating are directly related to the

461   period of the grating, and this includes a triangular-profile grating such as used by Yaroshenko *et* al.[33]

462   Moreover, their work highlights the benefit of closer spacing of 10 cm between the phase grating and

463   analyzer grating. This is the opposite effect we are pursuing in our approach with a bi-prism array to

464   analyzer/structured detector of 1.06 m.

465   Periodic replication of a grating, which is the Talbot effect, results from the overlapping zero-order, 1st

466   order and -1st order diffracted beams, when those beams encounter a screen (detector). Yaroshenko *et* al.[33]

467   rightly calls for future work on sinusoidal amplitude gratings as those gratings produce only those

468   diffraction orders. Their triangular-shaped grating system clearly demonstrates periodic longitudinal

469   spacing of fringe visibility regions.

470   Our goal has been to keep the dimensions of our laboratory system within something that would fit a

471   present-day large bore X-ray CT scanner. Though our initial work is aimed at imaging small objects at

472   energies of 17.5 keV, we have performed calculations using Eq. (3) to see how the parameters of the bi-

473   prism system would change at higher X-ray energies. For example, if we were to image at 59 keV, because

474   of the change in refraction index decrement at higher energies, we would have to modify the material of the

475   bi-prism to something like nickel in Table 1 to obtain reasonable fringe visibility at 1.19 m from the bi-

476   prism array with a fringe separation of 3.69 μm.

477   Recent advances in grating fabrication techniques[34,35] alleviate some concerns regarding high-energy X-

478   ray phase contrast imaging. The pattern height of our laboratory G_0 grating is 24 microns, however 200

479   microns are now available, which could be available for higher energies. Much of the X-ray flux is

480   absorbed by G_0. Thus, with higher energies the thicker G_0 grating will have its effect on flux. However,

481   current CT tube technology, can operate at >100 kW for the scan duration necessary to acquire clinical

482   tensor tomographic data including attenuation, phase, and small angle scatter information.

483

4.A.3. Advantages of single shot approaches

There are single shot approaches,[7-11] which render phase, scattering, and attenuation data from single projection measurements without mechanical phase stepping measurements at each projections angle. The challenges of mechanical phase stepping are the need to obtain precise grating positing at multiple measurements per projection angle, whereas single shot approaches of data acquisition have shorter acquisition times and have better mechanical stability. However, the paper of von Teuffenbach *et al.*[36] does point out some negative aspects of previous single shot methods. For example, the reverse projection method[8] combines two interferograms taken exactly 180 degrees apart, which requires stability of the grating alignment for each view and gives only access to attenuation and differential phase-contrast projection images. The implementation of helical and cone beam tomography would be difficult. The Moiré analysis method[7] using a slight detuning of the interferometer suffers from loss in resolution in one dimension of the detector. The sliding window method[11] requires only a single interferogram per projection angle, but changes the grating position at each angular position. Missing interferograms are simply interpolated from adjacent projection angles. This works well for scans with high angular sampling.

The paper of von Teuffenbach *et al.*[36] compares three single shot approaches and demonstrate that it is possible to successfully reconstruct the linear attenuation coefficient, the refractive index and the linear diffusion coefficient (measure of small angle scatter attenuation) using a single measurement per projection angle without grating movements. In their paper using the interferogram-based statistical iterative reconstruction (IBSIR) method of data reconstruction, they compare: 1. an equidistant phase stepping (PS) acquisition where the analyzing grating was shifted by 1/3rd the grating period to obtain 3 measurements at 101 equal angular positions over 360° (identified as PS-IBSIR); 2. a sliding window phase-stepping (SW) acquisition that records only one measurement at each of 303 equal angular positions over 360° with the analyzing grating shifted by 1/3rd its period before the next acquisition (SW-IBSIR); and 3. a single shot

28

507 electromagnetic phase-stepping acquisition (SSEPS) recording a single image at each of 303 equal angular

508 positions over 360° with the position of the X-ray focal spot shifted from the previous acquisition before

509 each measurement (SSEPS-IBSIR). These three methods provided the same number of measurements. The

510 PS-IBSIR showed artifacts at sharp boundaries, probably due to the finer angular sampling even though the

511 same number of measurements. The SW-IBSIR and SSEPS-IBSIR methods showed similar X-ray

512 attenuation reconstruction with the SW-IBSIR method showing a slightly better contrast but showing more

513 artifacts in the phase reconstruction and somewhat more noise in the reconstruction of the scatter diffusion

514 coefficient. As can be seen from the author's very nice display of the Radon space sampling, even though

515 both methods provide the same number of angular sampling, the regular sampling of SW-IBSIR method

516 probably has more aliasing than the irregular sampling of the SSEP-SIBSIR method with the motion of the

517 X-ray focus spot. This Radon space sampling proposes interesting future investigations similar to those that

518 have been pursued using data compression with irregular Fourier space sampling in MRI.[37,38] The proposed

519 electronic phase stepping acquisition protocol incorporated into an interferometry system would be

520 perfectly suited for application with a clinical CT system because the required focal spot sweeping is

521 already available in most modern clinical CT systems and the technique is well suited for a continuously

522 rotating gantry; however, it supposes one could design an X-tube with electronic phase stepping without

523 focal spot sweeping.

524

525 **4.B. X-ray tube design for virtual electronic phase stepping**

526   Electromagnetic phase-stepping (EPS)[39] moves an electrical beam to move projections of the object

527 across the detector whereby the shifted images are combined to form pseudo phase-stepping images. Here

528 we propose a single-shot image acquisition approach using a novel X-ray source that provides for "virtual"

529 electronic phase stepping without focal spot sweeping. This approach involves using an X-ray

530 interferometer imaging system where the X-ray tube has multiple X-ray origins/spots. The tube is operated

531   in such a way that each spot is temporally modulated at differing frequencies, and spatially modulated to

532   form illumination beams with differing fringe locations as observed in the interferometer. Composite

533   images of an object acquired with the interferometer are subsequently separated according to the flashing

534   source that provided the illumination. This is accomplished via de-multiplexing transform processes[40] based

535   on the known temporal multiplexing transform of the source. After an alignment step, the isolated images

536   from a single composite image/exposure have the same view of the object but with different fringe

537   locations relative to a feature in the object. An isolated image group of each single view are then analyzed

538   to yield images representing the differential phase shift, attenuation, and X-ray scattering features of the

539   object. All of the X-ray optical components in the interferometer, either a Talbot-Lau or a biprism setup,

540   remain fixed and motionless.

541   A high-power X-ray tube design that does this full work of virtual electronic phase stepping during a

542   single exposure is illustrated in Fig. 14. Here, a binary multiplexing transform of the X-ray output is

543   conducted by normal tube operation. Multiple X-ray spots are generated on the side of a rotating and

544   linearly-translated cylinder. An X-ray window allows that G_0, is illuminated by each spot, but at slightly

545   different angles. The oscillating linear translation, about 2 Hz, carries the anode past separate, adjacent,

546   focused, and identical high-current electron guns. As the anode cylinder walls are patterned, either with

547   metal/insulator or with ridges/grooves, in varying stepped spatial periods, each X-ray spot turns on/off at

548   different frequencies.

549   Other multiplexing transforms can result from different patterning, which might work better with slower

550   detectors. Lower power tubes can control the electron guns independently to accomplish a similar

551   multiplexed X-ray tube output.

552
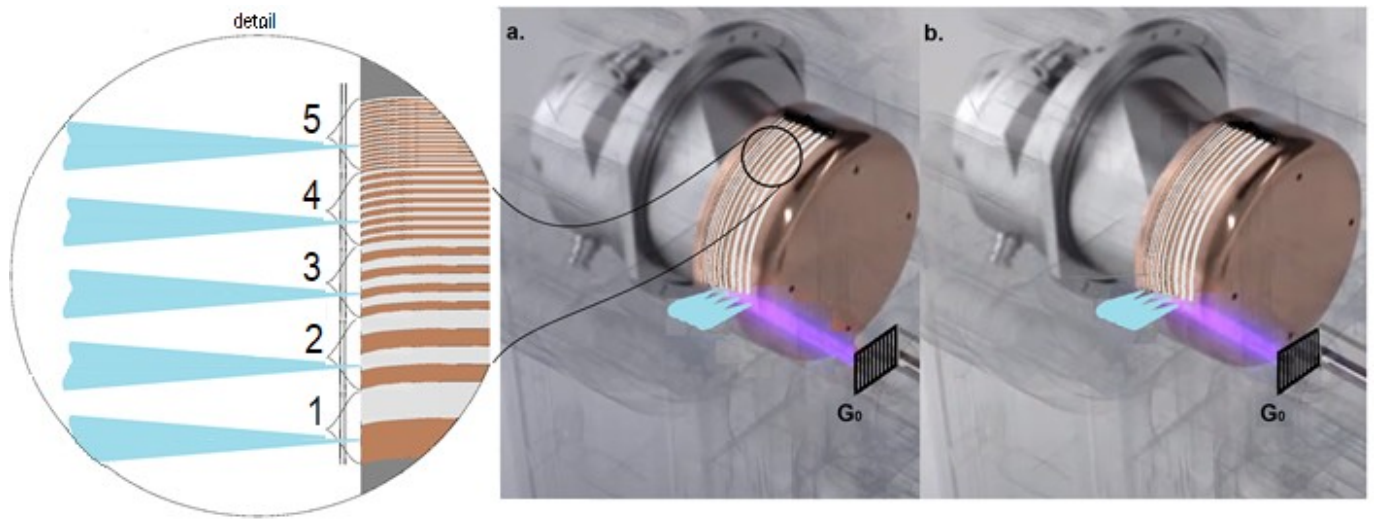
Fig. 14. Illustration of multiple-spot cylindrical rotating anode X-ray tube with oscillating translation for phase/dark-field single-shot data acquisition. (a.) Anode at minimum extension, (b.) Anode at maximum extension, **detail**: showing multiple spot tracks/flash rates 1.) Low frequency spot, 2.) Lower mid-frequency spot, 3.) Higher mid-frequency spot, 4.) High-frequency spot, 5.) Very high-frequency spot. (Image courtesy Rigaku Corp., Akishima-shi, Tokyo, Japan.)

5. CONCLUSION

563

564   Phase-contrast and dark-field X-ray CT for clinical human use will require advancements in X-ray optics,

565 X-ray sources, and X-ray detectors. As an alternative X-ray optical component, a Fresnel bi-prism array

566 adds to the set of tools available for the development of phase contrast imaging systems. Here, we present

567 one possible approach that is somewhat like an "inverse geometry Talbot-Lau" setup, but with improved

568 fringe visibility. Other bi-prism-based interferometry approaches are possible, including combinations with

569 phase gratings. We also present an advanced X-ray tube design that offers single-shot "virtual electronic

570 phase stepping." These two technologies, when combined with previously demonstrated structured-

571 scintillator detectors, can provide separate phase, dark-field, and attenuation signals without the need for

572 mechanical phase stepping. A system employing these components could be made to capture X-ray dark

573 field projections for direct tomographic tensor reconstruction of small angle scatter. The review of the

574 literature presents evidence of advancement in hardware (without grating phase stepping) and of new

575 algorithm developments that could provide fast single shot acquisition with mechanical simplicity

576 delivering less radiation exposure and faster acquisition times.

577 **ACKNOWLEDGEMENTS**

580

581 **CONFLICT OF INTEREST**

582   The authors have no conflict of interest.

583

584 **DATA AVAILABILITY**

585 Data distribution is available through an appropriate data sharing agreement between institutions.

<p>586   **REFERENCES**</p>

587   1. Momose A, X-ray phase imaging reaching clinical uses. *Phys Med*. 2020;79:93-102.

588   2. Doblas A, Saavedra G, Martinez-Corral M, Barreiro JC, Sanchez-Ortiga E, Llavador A, Axial

589   resonance of periodic patterns by using a Fresnel biprism. *J Opt Soc Am A*. 2013;30:140-148.

590   3. Ablett JM, Evans-Lutterodt K, Stein A, Hard x-rays Fresnel prisms: Properties and applications, in

591   Design and Microfabrication of Novel X-ray Optics II, A. A. Snigirev and D. C. Mancini, Eds.

592   Proceedings of SPIE, vol. 5539, August 2, 2004.

593   4. Gullberg GT, Fuller M, Shrestha U, Seo Y, Tensor tomography of dark field scatter using x-ray

594   interferometry with bi-prisms. 2017 IEEE Nuclear Science Symposium and Medical Imaging

595   Conference Record (NSS/MIC), Oct. 21 – 28, 2017, Atlanta, Georgia.

596   5. Sahlholm A, Svenonius O, Petersson S, Scintillator technology for enhanced resolution and contrast in

597   X-ray imaging. *Nuclear Instruments and Methods in Physics Research Section A: Accelerators,*

598   *Spectrometers, Detectors and Associated Equipment.* 2011;648:S16-S19.

599   6. Rutishauser S, Zanette I, Donath T, Sahlholm A, Linnros J, David C, Structured scintillator for hard x-

600   ray grating interferometry. *Appl Phys Lett*. 2011;98(17):171107 - 171107-3.

601   7. Seifert M, Gallersdörfer M, Ludwig V, Schuster M, Horn F, Pelzer G, Rieger J, Michel T, Anton G,

602   Improved reconstruction technique for Moiré imaging using an X-ray phase-contrast Talbot–Lau

603   interferometer. *J Imaging.* 2018;4(62):68-81.

604   8. Zhu P, Zhang K, Wang Z, Liu Y, Liu X, Wu Z, McDonald SA, Marone F, Stampanoni M, Low-dose,

605   simple, and fast grating-based X-ray phase-contrast imaging. *Proc Natl Acad Sci*. 2010;107:13576–81.

606   9. Bennett EE, Kopace R, Stein AF, Wen H, A grating-based single-shot X-ray phase contrast and

607   diffraction method for in vivo imaging. *Med Phys*. 2010;37:6047–54.

608 10. Wen HH, Bennett EE, Kopace R, Stein AF, Pai V, Single-shot X-ray differential phase-contrast and

609   diffraction imaging using two-dimensional transmission gratings. *Opt Lett.* 2010;35:1932–4.

610 11. Zanette, I., Bech, M. & Rack, A. Trimodal low-dose X-ray tomography. *Proceedings of the National*

611   *Academy of Sciences* 2012;109:10199–204.

612 12. Liu H, Cartwright AN, Basaran C, Sensitivity improvement in phase shifted moiré interferometry using

613   1D continuous wavelet transform image processing. *Opt Eng.* 2003;42:2646–52.

614 13. Liu H, Cartwright AN, Basaran C, Moiré interferogram phase extraction: A ridge detection algorithm

615   for continuous wavelet transforms. *Appl Opt*. 2004;43(41):850-857.

616 14. Bevins N, Zambelli J, Li K, Qi Z, Multicontrast x-ray computed tomography imaging using Talbot-Lau

617   interferometry without phase stepping. *Med Phys.* 2012:39:424-428.

618 15. Marschner M, Willner M, Potdevin G, Fehringer A, Noël PB, Pfeiffer F, Herzen J, Helical X-ray phase-

619   contrast computed tomography without phase stepping. *Sci Rep*. 2016;6:23953.

620 16. Itoh H, Nagai K, Sato G, Yamaguchi K, Nakamura T, Kondoh T, Ouchi C, Teshima T, Setomoto Y,

621   Den T, Two-dimensional grating-based X-ray phase-contrast imaging using Fourier transform phase

622   retrieval. *Opt Express.* 2011;19(4):3339-46.

623 17. Miao H, Panna A, Gomella AA, Bennett EE, Znati S, Chen L, Wen H, A universal moiré effect and

624   application in X-ray phase-contrast imaging. *Nat Phys.* 2016;12:830–4.

625 18. Suzuki Y, Takeuchi A, Hard x-ray holographic microscopy using refractive prism and Fresnel zone plate

626   objective. *Rev Sci Instrum.* 2005;76:093702.

627 19. Isakovic F, Stein A, Warren JB, Sandy AR, Narayanan S, Sprung M, Ablett JM, Siddons DP, Metzler

628   M, Evans-Lutterodt K, A bi-prism interferometer for hard X-ray photons. *J Synchrontron Radiat*.

629   2010;17:451-5.

630 20. Zverev D, Snigireva I, Kohn V, Kuznetsov S, Yunkin V, Snigirev A, X-ray phase-sensitive imaging

631   using a bilens interferometer based on refractive optics. *Opt Express* 2020;28(15):21856.

632 21. Lang AR, Makepeace APW, Production of synchrotron x-ray biprism interference patterns with control

633   of fringe spacing. *J Synchrotron Rad*. 1999;6:59–61.

634 22. Jacques V, Wu E, Toury T, Treussart F, Aspect A, Grangier P, Roch J-F, Single-photon wavefront-

635   splitting interference: An illustration of the light quantum in action. *Eur Phys J D* 2005;35:561–565.

636 23. Jacques V, Lai ND, Dréau A, Zheng D, Chauvat D, Treussart F, Grangier P, Roch J-F, Illustration of

637   quantum complementarity using single photons interfering on a grating. *New J Phys*. 2008;10:123009.

638 24. Missiroli GF, Pozzi G, Valdri U, Electron interferometry and interference electron microscopy. *J Phys*

639   *E Sci Instrum*. 1981;14:649–71.

640 25. Jenkins FA and White HE, Fundamentals of Optics (Fourth Edition) 2011 (McGraw Hill).
641

642 26. Mamyrbayev T, Ikematsu K, Meyer P, Ershov A, Momose A, and Mohr J, Super-resolution scanning

643   transmission X-ray imaging using single biconcave parabolic refractive lens array. *Sci Rep*. 2019; 9:

644   14366.

645 27. The Center for X-ray Optics Database, Lawrence Berkeley National Lab,

646   https://henke.lbl.gov/optical_constants/.

647 28. Serguei Kuznetsov, X-Ray Optics Calculator, IMT RAS, Chernogolovka, Russia, http://purple.iptm.ru/

648   xcalc/xcalc_mysql/ref_index.php.

649 29. Thuering T, Barber WC, Seo Y, Alhassen F, Iwanczyk JS, Stampanoni M, Energy resolved X-ray

650   grating interferometry, *Appl Phys Lett*. 2013;102:191113.

651 30. Donath T, Chabior M, Pfeiffer F, Bunk O, Reznikova E, Mohr J, Hempel E, Popescu S, Hoheisel M,

652   Schuster M, Baumann J, David C, Inverse geometry for grating-based x-ray phase-contrast imaging. *J*

653   *Appl Phys*. 2009;106:054703.

654 31. Momose A, Kuwabara H, Yashiro W, X-ray phase imaging using Lau effect. *Appl Phys Express*

655   2011;4:066603.

656   32. Tao W, Sung Y, Kim SJW, Huang Q, Gullberg GT, Seo Y, Fuller M. Tomography of dark field scatter

657   using single-exposure Moiré fringe analysis of x-ray bi-prism interferometry – A simulation study. *Med*

658   *Phys.* July 2021;00:1-19. DOI:10.1002/mp.15134.

659   33. Yaroshenko A, Bech M, Potdevin G, Malecki A, Biernath T, Wolf J, Tapfer A, Schüttler M, Meiser J,

660   Kunka D, Amberger M, Mohr J, Pfeiffer F, Non-binary phase gratings for x-ray imaging with a

661   compact Talbot interferometer. *Optics Express*. 2014;22(1): 547-56.

662   34. Finnegan P, Hollowell AE, Arrington CL, Dagel AL. High aspect ratio anisotropic silicon etching for x-

663   ray phase contrast imaging grating fabrication. *Mater Sci Semicond Process*. 2019;92:80-5.

664   35. Hollowell AE, Arrington CL, Finnegan P, Musick K, Resnick P, Volk S, Dagel AL. Double sided

665   grating fabrication for high energy X-ray phase contrast imaging *Mater Sci Semicond Process*.

666   2019;92:86-90.

667   36. von Teuffenbach M, Koehler T, Fehringer A, Viermetz M, Brendel B, Herzen J, Proksa R, Rummeny

668   EJ, Pfeiffer F, Noël PB, Grating-based phase-contrast and dark-field computed tomography: a single-

669   shot method. *Scientific Reports* 2017;7.1: 1-8.

670   37. Lustig M, Donoho DL, Pauly JM, Sparse MRI: The application of compressed sensing for rapid MR

671   imaging. *Magn Reson Med*. 2007;58(6):1182–95.

672   38. Lustig M, Donoho DL, Santos JM, Pauly JM, Compressed sensing MRI. *IEEE Signal Processing*

673   *Magazine* 2008;Mar:72-82.

674   39. Miao H, Chen L, Bennett EE, Adamo NM, Gomella AA, DeLuca AM, Patel A, Morgan NY, Wen H,

675   Motionless phase stepping in X-ray phase contrast imaging with a compact source. *Proc Natl Acad Sci*.

676   2014;111(52):19268-72.

677   40. Zhang J, Yang G, Lee Y, Chang S, Lu JP, Zhou O, Multiplexing radiography based on carbon nanotube

678   field emission x-ray technology. Proceedings Volume 6510, Medical Imaging 2007: *Physics of Medical*

679   *Imaging*; 65100W (2007).

FIGURE CAPTIONS

681   Fig. 1. (a) Schematic diagram of an X-ray grating interferometry system. (b) Talbot-Lau carpet.

682   Illuminating plane wave passes through a grating producing a fringe pattern with replicating amplified

683   fringe patterns at regular distances from the sources produced by the grating. At $Z_T/2$ there is a secondary

684   Talbot image and at Z_T a replication of the original Talbot image that emerged from the grating. At $Z_T/4$

685   there is a double frequency fractional image and increased frequency of images at less fractional distances.

686   (Modified from Wikipedia: https://en.wikipedia.org/wiki/Talbot_effect.)

687

688   Fig. 2. Schematic diagram of an X-ray bi-prism interferometry system. (a) Operation of a Fresnel X-ray

689   bi-prism, (b) experimental setup with multiple X-ray origins each producing fringes in resonant position,

690   and (c) detail of production of Moiré fringes via a tilted grating G_2 at the detector. Our intention is to

691   eliminate the G_2 granting and instead use only a detector/scintillator with small hexagonal elements to

692   produce the Moiré fringe pattern. (Modified from our earlier publication.[4])

693

694   Fig. 3. X-ray beam deflection by a bi-prism illustrating the distance d between the two virtual coherent

695   point sources produced by a bi-prism. (Copied from The Fresnel Biprism, David-Alexander Robinson and

696   Jack Denning; Daniel Tanner 08332461; 10th December 2009.)

697

698   Fig. 4. Lab setup of the bi-prism interferometry system at UCSF. The bi-prism interferometry system

699   includes a molybdenum-target X-ray tube operating at 35 kVp with predominate energy of the 17.5 keV

700   characteristic line (designed energy/wavelength). Shown also is a gold source grating with 0.8 μm apertures

701   separated by 4.8 μm, a bi-prism array made of plastic/epoxy photoresist material (SU-8), and a Stanford

702   Photonics iCCD camera.

703

704   Fig. 5. X-ray beam deflection by bi-prism. Here is given the expression for the angle α of the beam

705   deflection and the distance d between the two virtual coherent point sources produced by a bi-prism. δ is

706   the refraction index decrement. Notice the difference in refraction between X-rays and light. (Modified from

707   Chegg Study, www.x-ray-optics.de, and researchgate.net)

708

709   Fig. 6. Density plot of a fringe pattern for 25-point sources with 1 bi-prism. The amplification of the

710   interference pattern is repeated at non-periodic distances away from the plane of the bi-prism. For the

711   calculation we set $\lambda = 7.1 \times 10^{-11}$ m (17.5 keV), $I_p = 1/\Delta^2$, $\Delta = 7.00 \times 10^{-7}$ m, $\alpha = \delta \tan(\chi)$, $\delta = 1.58 \times 10^{-6}$

712   (silicon), $\chi = 82°$, $\eta = 0.4$ m, and $x_0 = 36.7 \mu$m. This figure is modified with new parameters from that of our

713   previous publication.[4]

714

715   Fig. 7. Density plot of a fringe pattern for 17-point sources with 1 bi-prism for a different set of

716   parameters than those in Fig. 6. For the calculation we set $\lambda = 7.1 \times 10^{-11}$ m (17.5 keV), $I_p = 1/\Delta^2$,

717    $\Delta = 8.00 \times 10^{-7}$ m, $\alpha = \delta \tan(\chi)$, $\delta = 8.7 \times 10^{-7}$ [plastic/epoxy photoresist material (SU-8)], $\chi = 85.3°$,

718    $\eta = 0.53$ m, and $x_0 = 4.8 \mu$m, $x_b = 10 \mu$m. There is a fringe separation of 1.09×10^{-5} m at $z = ¿1.2$ m.

719

720   Fig. 8. Density plot of a fringe pattern for 17-point sources with 1 bi-prism for the same set of parameters

721   as those in Fig. 7, except x_0 was changed from $x_0 = 4.8 \mu$m to $x_0 = 36.7 \mu$m For the calculation:

722    $\lambda = 7.1 \times 10^{-11}$m (17.5 keV), $I_p = 1/\Delta^2$, $\Delta = 8.00 \times 10^{-7}$ m, $\alpha = \delta \tan(\chi)$, $\delta = 8.7 \times 10^{-7}$ [plastic/epoxy

723   photoresist material (SU-8)], $\chi = 85.3°$, $\eta = 0.53$ m, and $x_0 = 36.7 \mu$m, $x_b = 10 \mu$m.

724

725   Fig. 9. Density plot of a fringe pattern for 17-point sources with 101 bi-prism for the same set of

726   parameters as in Fig. 7. For the calculation we set $\lambda = 7.1 \times 10^{-11}$m (17.5 keV), $I_p = 1/\Delta^2$, $\Delta = 8.00 \times 10^{-7}$ m,

727   $\alpha = \delta \tan(\chi)$, $\delta = 8.7 \times 10^{-7}$[plastic/epoxy photoresist material (SU-8)],$\chi = 85.32°$, $\eta = 0.53$ m, and

728   $x_0 = 4.8\,\mu$m, $x_b = 10\,\mu$m. There is a fringe separation of 1.00×10^{-5} m at $z = \dot{c}1.05$ m.

729

730   Fig. 10. Sensitivity as a function of bi-prism angle χ for X-ray source energies of (a) $\lambda = 7.1 \times 10^{-11}$m

731   (17.5 keV) and (b) $\lambda = 2.14 \times 10^{-11}$m (59 keV). For the calculation we set $N_s = 1$, $N_b = 1$, $I_p = 1/\Delta^2$,

732   $\Delta = 8.00 \times 10^{-7}$ m, $\delta = 8.7 \times 10^{-7}$ (SU-8), $\eta = 0.53$ m, $x = 0.000001$ m, and $z = 1$ m.

733

734   Fig. 11. Intensity as a function of point source size Δ : $Intensity = \dfrac{13736\,\Delta + \sin(626988\,\Delta)}{8\,\Delta}$. For the

735   calculation we set $N_s = 17$, $N_b = 101$, $I_p = 1/\Delta^2$, $\delta = 8.7 \times 10^{-7}$ (SU-8), $\chi = 85.32°$, $\eta = 0.53$ m, $x_0 = 4.8\,\mu$m,

736   $x_b = 10\,\mu$m, $x = 0$ m, and $z = 1.06$ m.

737

738   Fig. 12. Intensity as a function of separation between point sources x_0. For the calculation we set $N_s = 17$,

739   $N_b = 101$, $I_p = 1/\Delta^2$, $\Delta = 8.00 \times 10^{-7}$ m, $\delta = 8.7 \times 10^{-7}$ (SU-8), $\chi = 85.32°$, $\eta = 0.53$ m,$x_b = 10\,\mu$m, $x = 0$ m,

740   and $z = 1.06$ m.

741

742   Fig. 13. Proposed cone-beam tensor tomography system. The X-ray source and optics rotate around an

743   axis aligned to the center of an area detector with hexagonally segmented crosstalk-free scintillation

744   elements. The components are mounted on a revolving gantry (for clarity, not shown here). X-ray scatter

745   data is captured for three specific orientations 120° apart for every angular view.

746

747   Fig. 14. Illustration of multiple-spot cylindrical rotating anode X-ray tube with oscillating translation for

748   phase/dark-field single-shot data acquisition. (a.) Anode at minimum extension, (b.) Anode at maximum

749   extension, **detail**: showing multiple spot tracks/flash rates 1.) Low frequency spot, 2.) Lower mid-

750   frequency spot, 3.) Higher mid-frequency spot, 4.) High-frequency spot, 5.) Very high-frequency spot.

751   (Image courtesy of Rigaku Corp., Akishima-shi, Tokyo, Japan.)